Enhanced localized plasmonic characteristics based on coaxial defective-disk and ring structures

2015 J. Opt. 17 075101

(http://iopscience.iop.org/2040-8986/17/7/075101)

IOP Publishing Journal of Optics
J. Opt. **17** (2015) 075101 (6pp) doi:10.1088/2040-8978/17/7/075101

Enhanced localized plasmonic characteristics based on coaxial defective-disk and ring structures

Minghui Yuan[1], Changying Chen[1], Lin Chen[1,3], Ling Wei[1], Bo Fang[1,2], Zhaoxiang Cheng[1] and Yiming Zhu[1,3]

[1] Shanghai Key Lab of Modern Optical System, Engineering Research Center of Optical Instrument and System, Ministry of Education, University of shanghai for Science and Technology, 516 Jungong Road, Shanghai 200093, People's Republic of China
[2] College of Metrology and Measurement Engineering, China Jiliang University, Hangzhou 310018, People's Republic of China
[3] Cooperative Innovation Centre of Terahertz Science, University of Electronic Science and Technology, Chengdu, 611731, People's Republic of China

E-mail: linchen@usst.edu.cn and ymzhu@usst.edu.cn

Received 9 February 2015, revised 23 April 2015
Accepted for publication 29 April 2015
Published 10 June 2015

Abstract
We have illustrated the localized plasmonic properties on the terahertz region based on a coaxial disk and ring structure (DRS) and a defective-disk and ring structure (DDRS). Two resonances can be observed in these coaxial structures, which arise from the anti-bonding and bonding resonance hybridization. Compared with DRS, an enhanced localized plasmonic effect at a higher-frequency resonance is observed on the DDRS, which is owing to a new strong dipole mode evoked at the edge of the wedge-shaped slice. Moreover, this higher-frequency localized plasmonic resonance of the DDRS could be further enhanced by increasing the depth of the wedge-shaped slice due to the coupling between the dipole resonance of the deeper wedge-shaped slice and the outer ring. Therefore, by using higher-order enhanced localized plasmonic characteristics, the designed DDRS is promising in sensing, spectroscopy and slow light effect.

Keywords: metamaterials, electromagnetic optics, resonance

1. Introduction

Metamaterials have greatly expanded the range of electromagnetic properties exhibited by naturally occurring materials. Owing to the arrival of metamaterials, it enables the possibilities to achieve optical magnetism [1], negative refraction [2], super-lenses [3], Fano resonance [4, 5], transformation optics [6], filters [7, 8] and novel biosensors [9]. Furthermore, metamaterials own unusual phenomenon absent in natural materials, such as realizing slow light [10, 11] and even fabricating topological insulators [12]. In addition, localized surface plasmons (LSP) have been found in the terahertz (THz) region with disk or ring structures analogous to the particle model in a classic system. Zhang *et al* have researched the LSP properties of the subwavelength disk and ring coaxial structure (DRS), which exhibits a low-frequency anti-bonding mode and a high-frequency bonding mode [13, 14]. As its special plasmon hybridization properties, the coaxial geometries are promising in sensing and spectroscopy.

Although plasmonic defective nanodisk structures were presented in the optical range [15, 16] and focus on Fano resonance for grazing incidence, in this paper, on the basis of the structure in [13], we propose a coaxial defective-disk and ring structure (DDRS), which focuses on the coupling between the inner defective disk and the outer ring in the DDRS for normal incidence in THz range. When a defective component is embedded in the disk, an improved dipole mode at a higher frequency in the wedged-shaped slice is produced, which leads to an enhanced coupling between the inner disk (defective disk) and the outer ring. Moreover, this high-frequency localized plasmonic resonance of the DDRS could be

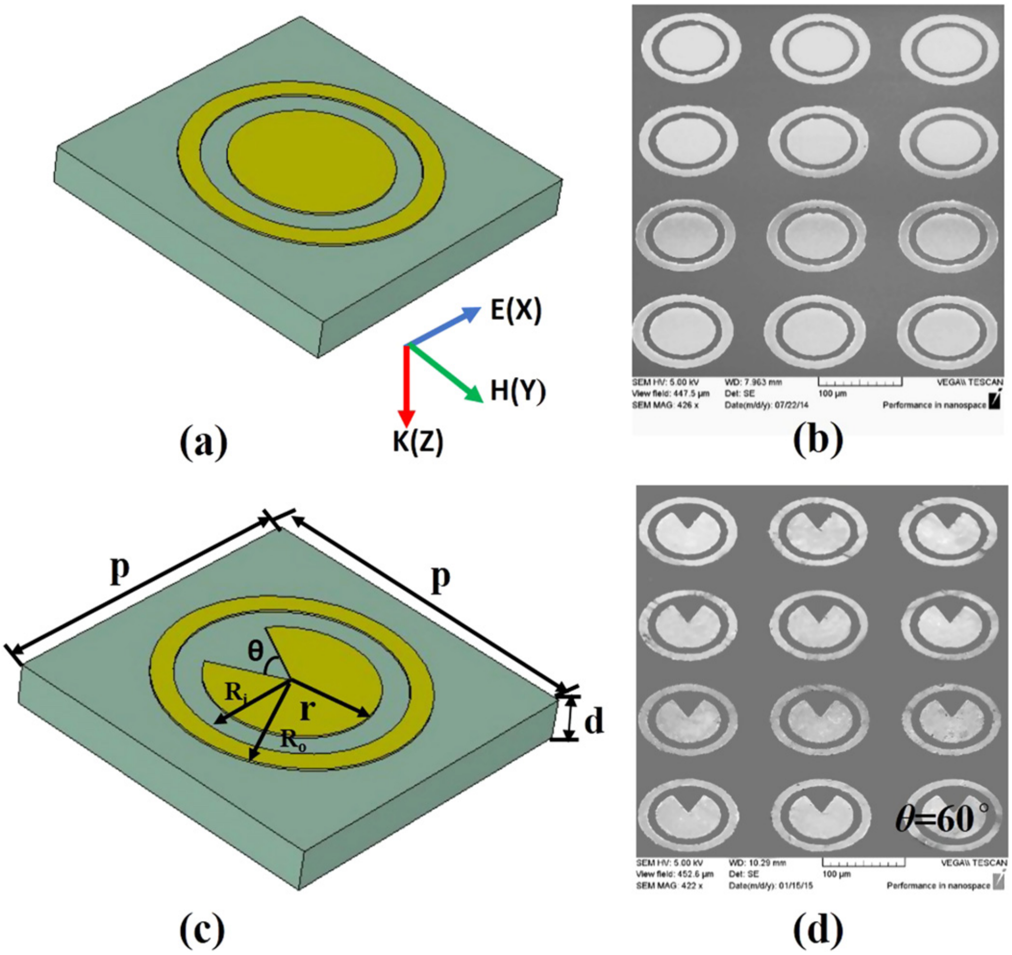

Figure 1. (a) The planar structure of DRS. The inner radius of ring $R_i = 50\ \mu$m, the outer radius of the ring $R_o = 60\ \mu$m, the disk radius $r = 38\ \mu$m, the period of the unit cell $p = 80\ \mu$m, and the thickness of silicon substrate $d = 500\ \mu$m. The thickness of the aluminum microstructure is 200 nm. The external electric field is along the x axis direction. (b) The SEM photograph of DRS. (c) The planar structure of DDRS, the defective angle $\theta = 60°$. (d) The SEM photograph of DDRS.

further enhanced by increasing the depth of the wedge-shaped slice. Compared with DRS, the DDRS exhibits an enhanced localized plasmonic effect at a higher-frequency resonance, which could be widely used in THz sensing, spectroscopy or slow light effect.

2. Fabrication of the samples

The geometric parameters of the unit cell are depicted in figures 1(a) and (c). The inner radius of ring $R_i = 50\ \mu$m, the outer radius of ring $R_o = 60\ \mu$m, the disk radius $r = 38\ \mu$m, the period of the unit cell $p = 80\ \mu$m, and the thickness of the silicon substrate $d = 500\ \mu$m. The defective angle $\theta = 60°$. The planar metamaterial samples were fabricated using conventional lithography followed by magnetron sputtering coating with a layer of 200 nm-thick aluminum with a conductivity of $\sigma_{\mathrm{Al}} = 3.56 \times 10^7$ S m^{-1} (behaves almost like a perfect conductor compared to the visible region [17]) on a low-loss n-type silicon substrate (relative permittivity $\varepsilon_{\mathrm{si}} = 11.9$) with a thickness of 500 μm [18, 19]. Figures 1(b) and (d) show the scanning electron microscope (SEM) photographs of the experimental sample with DRS and DDRS. The planar metamaterial samples were measured by a THz time domain spectroscopy (THz-TDS) system [20–22]. Furthermore, a normal incident beam with electric field E parallels the x axis.

3. Experiments and discussion

Here we start our discussion with the case of DRS, as illustrated in figure 2(a). There are two resonances detected, with one being a sharp and strong resonance at 0.37 THz (marked as I) and the other is a broad resonance located at 0.61 THz (marked as III). A sharp transmission peak (0.49 THz) is observed between those two resonance dips. The experimental (black line) and simulated (red line) transmission spectra fit very well. Figure 2(b) shows the experimental (black line) and simulated (red line) transmission spectra of the DDRS, which also show two resonance dips (0.37 THz and 0.56 THz) and a transparency peak (0.46 THz). Compared with the transmission response of the DRS, the transmission spectrum of the DDRS presents an enhanced LSP

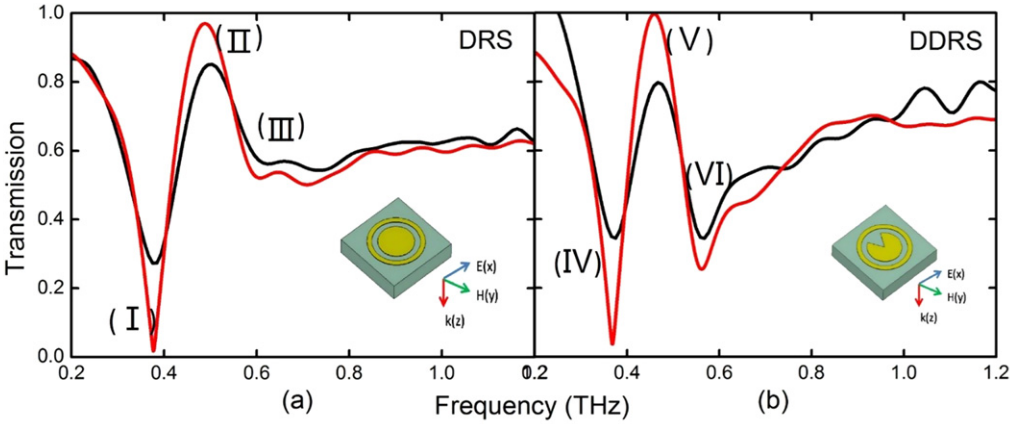

Figure 2. Measured (black line) and simulated (red line) transmission spectra of (a) DRS and (b) DDRS.

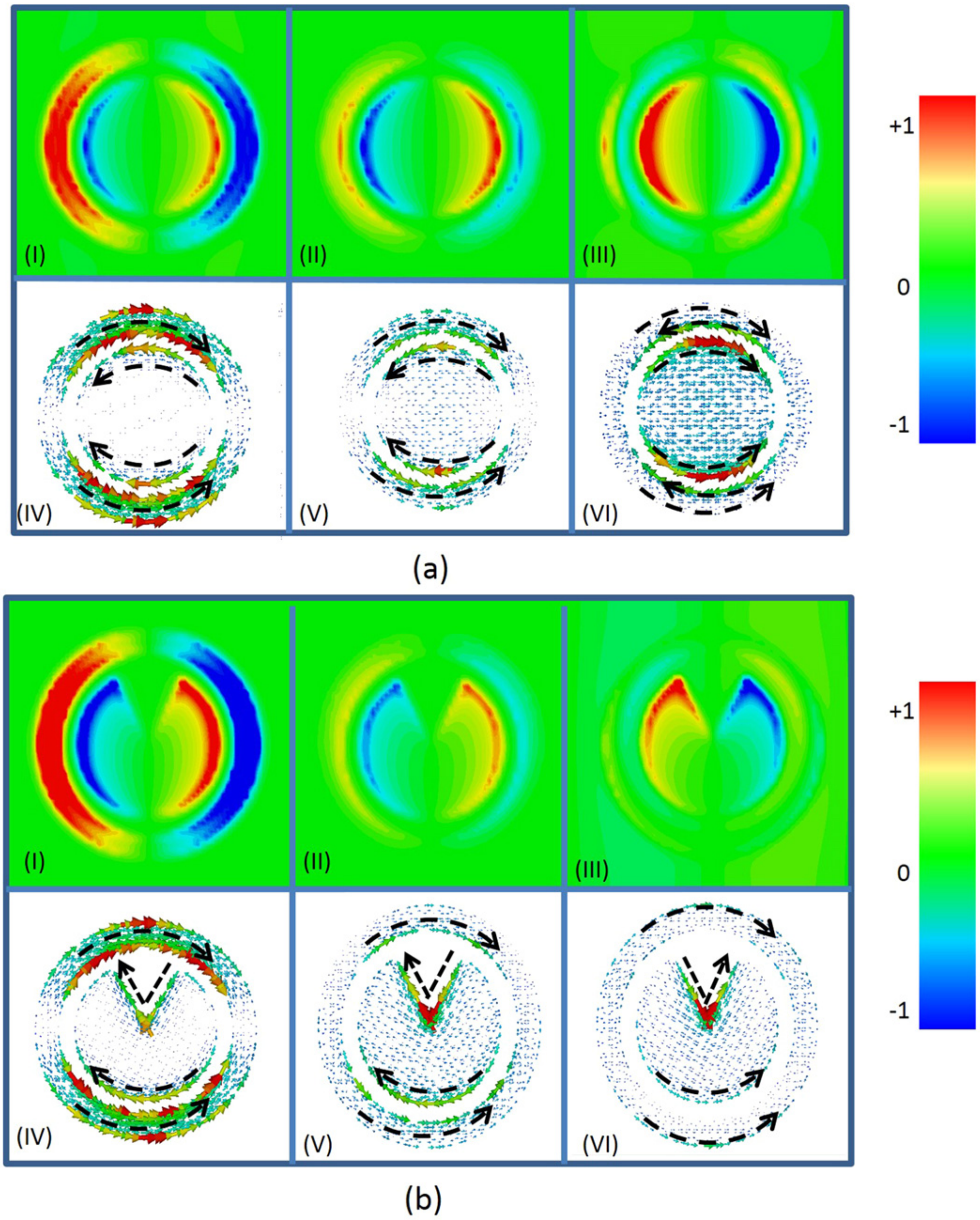

Figure 3. The electric field and surface current density distributions of (a) DSR and (b) DDSR. (I) (IV), (II) (V) and (III) (VI) correspond to mark I, II and III.

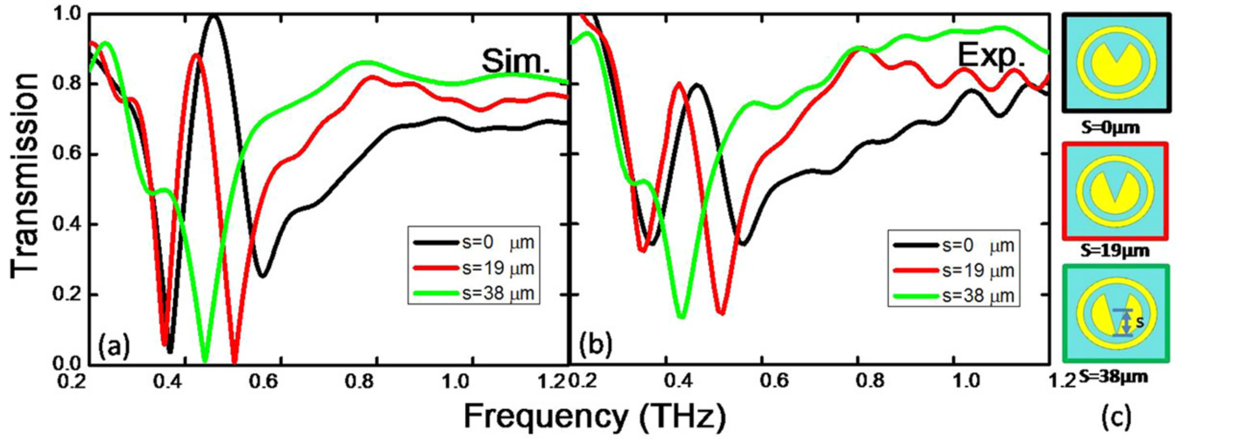

Figure 4. (a) Simulated and (b) measured transmission spectra of DDRS with different wedge-shaped slice depth s. (c) Images of DDRS with different depth s.

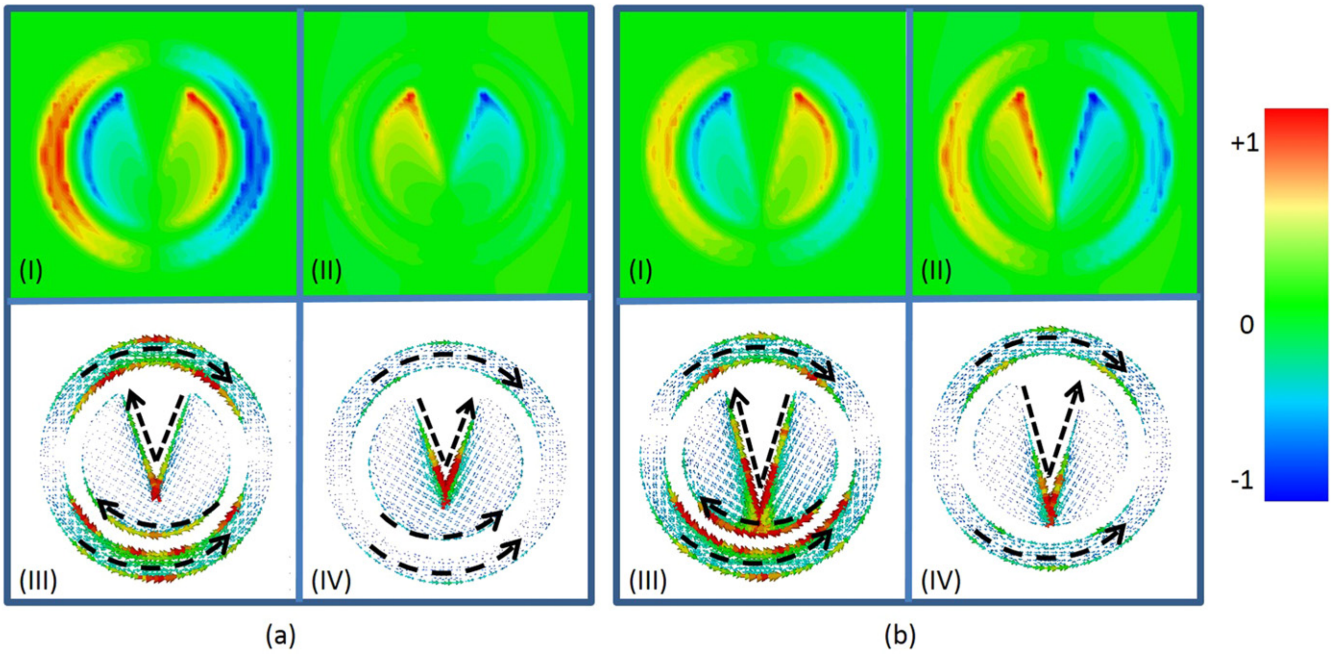

Figure 5. The electric field and surface current density distributions of the DDSR at the low-frequency resonance dip ((I) and (III)) and high-frequency resonance dip ((II) and (IV)) with wedge-shaped slice depth (a) $s = 19$ μm and (b) $s = 38$ μm.

effect, especially in the high-frequency resonance dip (III), and a sharper transparency peak is also observed [23].

To clarify the special resonance mechanism of the DRS and DDRS, electric field and surface current distributions are given in figure 3. In figure 3(a), we present the electric fields and surface current density distributions in the subwavelength coaxial DRS at frequencies corresponding to the resonant features of I, II and III. The resonance dips of I and III are evoked by a predominantly dipole mode in the outer ring and inner disk, respectively. The low-frequency resonance (I) can be traced as an anti-bonding mode due to inverse surface currents between the ring and disk, as presented in figure 3(a) (I) and (IV). While the identical surface currents in figure 3(a) (III) and (VI) exhibit that, the high-frequency dip (III) is a bonding mode. It is notable that the surface currents on the outside part of the ring are in the same direction of the inner disk, and both are evoked by the incident electric field. However, the surface currents on the inside part of the ring and disk are opposite, because the surface currents on the disk induce the opposite direction currents on the inside part of the ring. At the transmission peak II, however, the ring and disk appear to be excited equally, while the induced currents in the inner disk and outer ring oscillate in the opposite phase, yielding a trapped mode, as illustrated in figure 3(a) (II) and (V). The scattered electromagnetic fields produced by such current configurations are weak, which reduces coupling to free space. Consequently, as the coupling between bonding mode and anti-bonding mode is created, the strength of the induced currents can reach very high values and therefore result in a sharp transmission peak. The electric field and surface current distributions of the DDRS are exhibited in figure 3(b). The resonance characteristic of the low-frequency resonance dip (IV) is a typical anti-bonding mode, which is similar to the low-frequency resonance dip (I) of the DRS, as exhibited in figure 3(b) (I) and (IV). However, at the high-frequency resonance dip (VI), a uniform current distribution emerges and more energies concentrate on the tip of the wedge-shaped slice, as illustrated in figure 3 (III) and (VI). It is notable that as the disk's symmetry breaks, a dipole mode emerges at the edge of the wedge-shaped slice and the original dipole mode in the disk becomes weak, which lead to an enhanced resonance at the high-frequency dip (see as figure 3(b) (III) and (VI)). Compared with the non-defective coaxial disk and ring structure, the bonding mode at the high-frequency dip is stronger, which is due to the enhanced coupling between the dipole resonance of the wedge-shaped slice and the dipole resonance of the outer ring. Figure 3(b) (II) and (V) are the electric field and surface current distributions at the transparency peak (IV); the inhomogeneous energy distributions also can be found. Therefore, as a defective angle $\theta = 60°$ is embedded in the disk, the symmetry of the disk is broken and a stronger dipole mode in the defective disk emerges, which lead to an enhanced resonance of the disk. Then the coupling between the inner disk (defective disk) and outer ring is strengthened, and finally an improved LSP effect is observed.

To further clarify the coupling mechanism between the defective disk and ring, we investigate the transmission properties of the DDRS with different wedge-shaped slice depth s. Figures 4(a) and (b) are the simulated and measured transmission spectra when $s = 0\,\mu$m (black line), $s = 19\,\mu$m (red line) and $s = 38\,\mu$m (green line), and figure 4(c) is the image of the DDRS with different depth s. With the increase of slice depth s, the intensity at the high-frequency resonance dip (bonding mode) is monotonously enhanced, and the resonance frequency is a red shift. Meanwhile, the intensity at the low-frequency resonance dip (anti-bonding mode) becomes weak gradually. The improved resonance intensity could increase the sensitivity and further enhance the performance in sensors.

To understand the resonance mechanisms, the electric field and surface current density distributions of the DDSR at the low-frequency resonance dip ((I) and (III)) and high-frequency resonance dip ((II) and (IV)) with different wedge-shaped slice depths ($s = 19\,\mu$m $s = 38\,\mu$m) are shown in figure 5. First, we study the resonance property at the high-frequency dip, which is mainly caused by the dipole mode of the inner defective disk. With an increasing wedge-shaped slice depth s from $0\,\mu$m to $38\,\mu$m, the resonance of the dipole mode in the wedge-shaped slice is monotonously strengthened. Meanwhile, the resonance red-shifts with increasing s due to an increased edge length of the wedge-shaped slice. These discussions are in accordance with the electric field and surface current distributions, as presented in figure 3(b) (III) (IV) ($s = 0\,\mu$m), figure 5(a) (II) and (IV) ($s = 19\,\mu$m) and figure 5(b) (II) (IV) ($s = 38\,\mu$m). Next, we try to explain the resonance effect of the low-frequency resonance dip, which is an anti-bonding mode with asymmetric surface currents in the outer ring and inner defective disk. The electric field and surface current distributions at the low-frequency resonance dip are given in figure 3(b) (III) (IV) ($s = 0\,\mu$m), figure 5(a) (II) and (IV) ($s = 19\,\mu$m) and figure 5(b) (II) (IV) ($s = 38\,\mu$m). On one hand, with the increasing of s, the resonance intensity of the ring's dipole mode with clockwise surface currents is nearly unchangeable. On the other hand, the intensity of the inner defective disk's dipole mode with anti-clockwise surface currents is strengthened gradually with increasing s. Therefore, an enhanced destructive interference is observed between the inner defective disk and outer ring and consequently results in a degrading resonance at the low-frequency dip.

4. Conclusion

In conclusion, we have illustrated a localized plasmonic characteristic based on the DDRS, which results from the combination of anti-bonding and bonding modes. When a defective angle is embedded in the inner disk, a higher-frequency enhanced LSP effect is observed. This is due to the break of symmetry, together with a stronger dipole mode in the wedge-shaped slice, which lead to an enhanced coupling between the inner disk (defective disk) and outer ring. The electric field and current distributions are given to depict their resonance mechanisms. Moreover, the localized plasmonic resonance intensity of the DDRS can be changed with different depths of the wedge-shaped slice. Compared with DRS, DDRS exhibits an enhanced localized plasmonic characteristic. Therefore, such enhanced localized plasmonic based on DDRS may be widely used in sensing, spectroscopy or slow light effect.

Acknowledgments

This work was partly supported by the National Program on Key Basic Research Project of China (973 Program, 2014CB339806), Basic Research Key Project (12JC1407100), Major National Development Project of Scientific Instrument and Equipment (2011YQ150021) (2012YQ14000504), National Natural Science Foundation of China (11174207) (61138001) (61205094) (61307126), Shanghai Rising-Star Program (14QA1403100), Program of Shanghai Subject Chief Scientist (14XD1403000), Hujiang Foundation of China (C14002), Zhejiang Key Discipline of Instrument Science and Technology (JL150505), and the New Century Excellent Talents Project from the Ministry of Education (NCET-12-1052).

References

[1] Yen T J, Padilla W J, Fang N, Vier D C, Smith D R, Pendry J B, Basov D N and Zhang X 2004 Terahertz magnetic response from artificial materials *Science* **303** 1494–6

[2] Smith D R, Pendry J B and Wiltshire M C 2004 Metamaterials and negative refractive index *Science* **305** 788–92

[3] Fang N, Lee H, Sun C and Zhang X 2005 Sub–diffraction-limited optical imaging with a silver superlens *Science* **308** 534–7
[4] Luk'yanchuk B, Zheludev N, Maier S, Halas N J, Nordlander P, Giessen H and Chong C T 2010 The Fano resonance in plasmonic nanostructures and metamaterials *Nat. Mater.* **9** 707–15
[5] Singh R, Al-Naib I, Cao W, Rockstuh C, Koch M and Zhang W 2013 The Fano resonance in symmetry broken terahertz metamaterials *IEEE Trans. Terahertz Sci. Technol.* **3** 820–6
[6] Pendry J B, Schurig D and Smith D R 2006 Controlling electromagnetic fields *Science* **312** 1780–2
[7] Chen L, Truong K V, Cheng Z X, Li Z and Zhu Y M 2014 Characterization of photonic bands in metal photonic crystal slabs *Opt. Commun.* **333** 232–6
[8] Chen L, Zhu Y M, Zang X F, Cai B, Li Z, Xie L and Zhuang S L 2013 Mode splitting transmission effect of surface wave excitation through a metal hole array *Light Sci. Appl.* **2** e60
[9] Chen H, Chan C T and Sheng P 2010 Transformation optics and metamaterials *Nat. Mater.* **9** 387–96
[10] Cubukcu E, Zhang S, Park Y S, Bartal G and Zhang X 2009 Split ring resonator sensors for infrared detection of single molecular monolayers *Appl. Phys. Lett.* **95** 043113
[11] Wu C, Khanikaev A B and Shvets G 2011 Broadband slow light metamaterial based on a double-continuum Fano resonance *Phys. Rev. Lett.* **106** 107403
[12] Khanikaev A B, Mousavi S H, Tse W K, Kargarian M, MacDonald A H and Shvets G 2013 Photonic topological insulators *Nat. Mater.* **12** 233–9
[13] Lu X and Zhang W 2009 Terahertz localized plasmonic properties of subwavelength ring and coaxial geometries *Appl. Phys. Lett.* **94** 181106
[14] Lu X, Han J and Zhang W 2011 Localized plasmonic properties of subwavelength geometries resonating at terahertz frequencies *IEEE J. Sel. Top. Quantum Electron.* **17** 119–29
[15] Liu T, Li J, Gao F, Han Q and Liu S 2013 Generation and manipulation of higher order Fano resonances in plasmonic nanodisks with a built-in missing sectorial slice *Europhys. Lett.* **104** 47009
[16] Fang Z, Cai J and Yan Z 2011 Removing a wedge from a metallic nanodisk reveals a fano resonance *Nano Lett.* **11** 4475–9
[17] Chen L, Cao Z Q, Ou F, Li H G, Shen Q S and Qiao H C 2007 Observation of large positive and negative lateral shifts of a reflected beam from symmetrical metal-cladding waveguides *Opt. Lett.* **32** 1432–4
[18] Cheng Z X, Chen L, Zang X, Cai B, Peng Y and Zhu Y 2015 Ultrathin dual-mode filtering characteristics of terahertz metamaterials with electrically unconnected and connected U-shaped resonators array *Opt. Commun.* **342** 20–5
[19] Cheng Z X, Chen L, Zang X F, Cai B, Peng Y and Zhu Y M 2015 Tunable plasmon-induced transparency effect based on self-asymmetric H-shaped resonators meta-atoms *J. Opt.* **17** 035103
[20] Chen L, Gao C, Xu J M, Zang X F, Cai B and Zhu Y M 2013 Observation of electromagnetically induced transparency-like transmission in terahertz asymmetric waveguide-cavities systems *Opt. Lett.* **38** 1379–81
[21] Chen L, Cheng Z, Xu J, Zang X, Cai B and Zhu Y 2014 Controllable multiband terahertz notch filter based on a parallel plate waveguide with a single deep groove *Opt. Lett.* **39** 4541–4
[22] Chen L, Xu J M, Gao C M, Zang X F, Cai B and Zhu Y M 2013 Manipulating terahertz electromagnetic induced transparency through parallel plate waveguide cavities *Appl. Phys. Lett.* **103** 251105
[23] Yu S W, Shi J H, Zhu Z, Liu R and Guan C Y 2013 Multi-peak electromagnetically induced transparency in concentric multiple-ring metamaterials *J. Opt.* **15** 075103